

Velocity-gauge Real-time Time-dependent Density Functional Tight-binding for Large-scale Condensed Matter Systems

Qiang Xu,[†] Mauro Del Ben,[‡] Mahmut Sait Okyay,[†] Min Choi,[†] Khaled Z.
Ibrahim,[‡] and Bryan M. Wong^{*,†}

[†]*Materials Science & Engineering Program, Department of Chemistry, and Department of
Physics & Astronomy, University of California-Riverside, Riverside, California 92521,
United States*

[‡]*Applied Mathematics & Computational Research Division, Lawrence Berkeley National
Laboratory, Berkeley, California 94720, United States*

E-mail: bryan.wong@ucr.edu, Website: <http://www.bmwong-group.com>

Abstract

We present a new velocity-gauge real-time, time-dependent density functional tight-binding (VG-rtTDDFTB) implementation in the open-source DFTB+ software package (<https://dftbplus.org>) for probing electronic excitations in large, condensed matter systems. Our VG-rtTDDFTB approach enables real-time electron dynamics simulations of large, periodic, condensed matter systems containing thousands of atoms with a favorable computational scaling as a function of system size. We provide computational details and benchmark calculations to demonstrate its accuracy and computational parallelizability on a variety of large material systems. As a representative example, we calculate laser-induced electron dynamics in a 512-atom amorphous silicon supercell to

highlight the large periodic systems that can be examined with our implementation. Taken together, our VG-rtTDDFTB approach enables new electron dynamics simulations of complex systems that require large periodic supercells, such as crystal defects, complex surfaces, nanowires, and amorphous materials.

1 Introduction

Real-time time-dependent density functional theory (rtTDDFT)¹⁻³ is a powerful approach for predicting the electron dynamics of quantum systems via solution of the time-dependent Kohn-Sham (KS) equations.⁴⁻¹³ rtTDDFT simulations can probe real-time electron dynamics in the presence of time-dependent external fields, which can be used to understand light-matter interactions and predict the linear/non-linear response of materials. The most common usage/implementation of rtTDDFT is for molecular (i.e., non-periodic) systems since the length gauge, which is used to calculate quantum dynamics in non-periodic systems, is relatively straightforward. However, the length-gauge formalism cannot be used for periodic systems since it breaks the translational symmetry of the Hamiltonian.¹⁴⁻¹⁶ For condensed matter systems, the time-dependent KS equations can be formally integrated under periodic boundary conditions¹⁷ using the velocity-gauge (VG) formalism,^{11,16} which has been used to probe laser-induced electron dynamics in a variety of solid-state systems.^{11,15,18-21}

Despite its broad applicability, the immense computational expense of rtTDDFT calculations prohibits its use for large material systems such as crystal defects, complex surfaces, heterostructures, and amorphous systems, which require large supercells. To enable these large-scale electron dynamics simulations, an alternate theoretical formalism with a low computational cost is required. To address this need, we present the first velocity-gauge real-time time-dependent density functional tight-binding (VG-rtTDDFTB) implementation in the open-source DFTB+ software package (<https://dftbplus.org>) for large-scale and long-time electron dynamics simulations with periodic boundary conditions. Our VG-rtTDDFTB implementation makes use of the density functional tight-binding (DFTB) formalism,^{22,23} which

is computationally efficient, relatively accurate, and scales extremely well with system size compared to full density functional theory (DFT).²⁴⁻²⁹

In this work, we derive the theoretical formalism and present a numerical implementation of VG-rtTDDFTB for electron dynamics simulations of large-scale condensed matter systems. Section 2 commences with a description of the VG-rtTDDFTB theoretical formalism. Section 3 provides computational details and benchmark calculations to demonstrate its accuracy and computational parallelizability on a variety of large material systems. Finally, we present an example of laser-induced electron dynamics in amorphous silicon to highlight the large periodic systems that can be examined with our approach, and we conclude with future prospects/applications of our VG-rtTDDFTB implementation.

2 Theoretical formalism

The time-dependent KS formalism with periodic boundary conditions in atomic units ($\hbar = e = m_e = 1$) is given by

$$i\frac{\partial}{\partial t}|\psi_{n\mathbf{k}}\rangle = \hat{H}_{\text{KS}}|\psi_{n\mathbf{k}}\rangle, \quad (1)$$

where $\psi_{n\mathbf{k}}$ is the wavefunction in the Bloch representation. In the long-wavelength limit, $\lambda \gg V^{1/3}$, where λ and V are the laser wavelength and volume of the simulation cell, respectively. Within this regime, the spatial variation of the electromagnetic field is negligible,^{30,31} which allows us to calculate macroscopic dielectric properties of solid-state systems.³² In the long-wavelength approximation, the VG-KS Hamiltonian is given by^{11,16,30}

$$\begin{aligned} \hat{H}_{\text{KS}} &= \frac{1}{2} \left[\hat{\mathbf{p}} + \frac{1}{c} \mathbf{A}(t) \right]^2 + \hat{V}_{\text{eff}}[\rho] \\ &= \frac{1}{2} \hat{\mathbf{p}}^2 + \hat{V}_{\text{eff}}[\rho] + \underbrace{\frac{1}{c} \mathbf{A}(t) \cdot \hat{\mathbf{p}} + \frac{1}{2c^2} |\mathbf{A}(t)|^2}_{\hat{H}_{\text{ext}}(t)}, \end{aligned} \quad (2)$$

where $\hat{\mathbf{p}}$ and \hat{V}_{eff} are the momentum and effective potential operators, respectively; c denotes

the speed of light in vacuum, $\rho(r) = \frac{1}{N_{\mathbf{k}}} \sum_{n\mathbf{k}}^{\text{occ.}} |\psi_{n\mathbf{k}}(r)|^2$ is the electron density, $N_{\mathbf{k}}$ is the number of k -points or the number of unit cells in the Born-von-Karman supercell used in the calculation,^{33,34} and $\hat{H}_{\text{ext}}(t)$ is the Hamiltonian containing the external vector potential, which is given by

$$\mathbf{A}(t) = -c \int_0^t \mathbf{E}(\tau) d\tau, \quad (3)$$

where \mathbf{E} is the external electric field; e.g., $\mathbf{E}(t) = \mathbf{E}_0 \delta(t)$ for a delta function “kick” field, and $\mathbf{E}(t) = \mathbf{E}_0 \cos(\omega t)$ corresponds to a monochromatic “laser” field with frequency ω . Note that the last term in Eq. (2) is a function of time that only gives rise to an overall phase factor of the form $e^{-i \int_0^t |A(\tau)|^2 d\tau / (2c^2)}$ in the time-dependent wavefunction.¹ This overall phase factor does not affect observables and density matrices in our implementation.

The self-consistent-charge density functional tight-binding (SCC-DFTB) formalism²² uses nonorthogonal pseudoatomic basis sets, $\{|\phi_{\mu}^{\zeta}\rangle\}$, and effective potentials in a two-center approximation. The collective index μ represents (I, l, m) such that $|\phi_{\mu}^{\zeta}\rangle$ denotes the orbital centered on the I th atom of the ζ th periodic cell image in real space with (l, m) angular momentum quantum numbers, where $\phi_{\mu}(\mathbf{r} - \mathbf{R}_I - \mathbf{L}_{\zeta}) = \langle \mathbf{r} | \phi_{\mu}^{\zeta} \rangle$, \mathbf{R}_I and \mathbf{L}_{ζ} are the positions of the I th atom and ζ th periodic image, respectively. The Bloch state in the SCC-DFTB formalism can be rewritten as

$$|\psi_{n\mathbf{k}}\rangle = \sum_{\zeta} \sum_{\mu=1}^{N_b} C_{n\mathbf{k}}^{\mu} e^{i\mathbf{k} \cdot \mathbf{L}_{\zeta}} |\phi_{\mu}^{\zeta}\rangle, \quad (4)$$

where N_b is the number of atomic basis functions in the unit cell. Combining Eqs. (1) and (4), the time-dependent DFTB equations in matrix form becomes

$$i \frac{\partial}{\partial t} \mathbf{C}_{n\mathbf{k}} = \mathbf{S}_{\mathbf{k}}^{-1} \mathbf{H}_{\mathbf{k}} \mathbf{C}_{n\mathbf{k}}, \quad (5)$$

where $\mathbf{C}_{n\mathbf{k}} = [C_{n\mathbf{k}}^1, C_{n\mathbf{k}}^2, \dots]^T$ is the coefficient vector of the $n\mathbf{k}$ th state. Alternatively, the

equation of motion for the k -dependent density matrices can be obtained from Eq.(5) as

$$i \frac{\partial}{\partial t} \mathbf{D}_{\mathbf{k}} = \mathbf{S}_{\mathbf{k}}^{-1} \mathbf{H}_{\mathbf{k}} \mathbf{D}_{\mathbf{k}} - \mathbf{D}_{\mathbf{k}} \mathbf{H}_{\mathbf{k}} \mathbf{S}_{\mathbf{k}}^{-1}, \quad (6)$$

where the k -dependent density matrix is defined as $\mathbf{D}_{\mathbf{k}} = \sum_n^{\text{occ.}} \mathbf{C}_{n\mathbf{k}} \mathbf{C}_{n\mathbf{k}}^\dagger$, and the elements of the k -dependent overlap ($\mathbf{S}_{\mathbf{k}}$) and Hamiltonian ($\mathbf{H}_{\mathbf{k}}$) matrices are given by

$$S_{\mathbf{k}}^{\mu\nu} = \sum_{\zeta} e^{-i\mathbf{k}\cdot\mathbf{L}_{\zeta}} \langle \phi_{\mu}^{\zeta} | \phi_{\nu}^0 \rangle = \sum_{\zeta} e^{-i\mathbf{k}\cdot\mathbf{L}_{\zeta}} \bar{S}^{\mu\nu}(\mathbf{L}_{\zeta}), \quad (7)$$

$$H_{\mathbf{k}}^{\mu\nu} = \sum_{\zeta} e^{-i\mathbf{k}\cdot\mathbf{L}_{\zeta}} \langle \phi_{\mu}^{\zeta} | \hat{H}_{\text{DFTB}} | \phi_{\nu}^0 \rangle = \sum_{\zeta} e^{-i\mathbf{k}\cdot\mathbf{L}_{\zeta}} \bar{H}^{\mu\nu}(\mathbf{L}_{\zeta}). \quad (8)$$

To numerically evaluate the VG Hamiltonian, the $\bar{H}^{\mu\nu}(\mathbf{L}_{\zeta})$ term in Eq. (8) can be rewritten within the SCC-DFTB approximation as

$$\bar{H}^{\mu\nu}(\mathbf{L}_{\zeta}) = \bar{H}_{(0)}^{\mu\nu}(\mathbf{L}_{\zeta}) + \bar{H}_{(2)}^{\mu\nu}(\mathbf{L}_{\zeta}) + \bar{H}_{\text{ext}}^{\mu\nu}(\mathbf{L}_{\zeta}), \quad (9)$$

where $\bar{H}_{(0)}^{\mu\nu}(\mathbf{L}_{\zeta}) \equiv \langle \phi_{\mu}^{\zeta} | \frac{1}{2} \hat{\mathbf{p}}^2 + \hat{V}_{\text{eff}}[\rho_0] | \phi_{\nu}^0 \rangle$, $\bar{H}_{(2)}^{\mu\nu}(\mathbf{L}_{\zeta})$, and $\bar{H}_{\text{ext}}^{\mu\nu}(\mathbf{L}_{\zeta})$ include contributions from the non-self-consistent-charge, self-consistent-charge (SCC), and external potential terms in DFTB, respectively. In SCC-DFTB, all of the $\bar{S}^{\mu\nu}(\mathbf{L}_{\zeta})$ and $\bar{H}_{(0)}^{\mu\nu}(\mathbf{L}_{\zeta})$ matrix elements are pre-tabulated using Slater-Koster techniques³⁵ with a reference density ρ_0 . The diagonal elements of $\bar{H}_{(0)}^{\mu\nu}(\mathbf{L}_{\zeta})$ correspond to the atomic orbital energies, and the off-diagonal elements are calculated in a two-centered approximation.²² The SCC-term $\bar{H}_{(2)}^{\mu\nu}(\mathbf{L}_{\zeta})$ is defined as

$$\bar{H}_{(2)}^{\mu\nu}(\mathbf{L}_{\zeta}) = \frac{1}{2} \bar{S}^{\mu\nu}(\mathbf{L}_{\zeta}) \sum_K (\gamma_{IK} + \gamma_{JK}) \Delta q_K, \quad (10)$$

where Eq. (10) depends on the Mulliken population $q_I = \frac{1}{2N_{\mathbf{k}}} \sum_{n\mathbf{k}}^{\text{occ.}} \sum_{\mu \in I, \nu} C_{n\mathbf{k}}^{\mu*} S_{\mathbf{k}}^{\mu\nu} C_{n\mathbf{k}}^{\nu} + c.c. = \frac{1}{N_{\mathbf{k}}} \sum_{\mathbf{k}} \sum_{\mu \in I} [\mathbf{D}_{\mathbf{k}} \mathbf{S}_{\mathbf{k}}]^{\mu\mu}$, and $\Delta q_I = q_I - Z_I$ is the charge fluctuation with respect to the ion charge Z_I . The μ th and ν th basis indices denote orbitals centered on the I th and J th atoms,

respectively. γ_{IJ} is defined as²²

$$\gamma_{IJ} = \frac{1}{R_{IJ}} - S(U_I, U_J; R_{IJ}), \quad (11)$$

where $R_{IJ} = |\mathbf{R}_I - \mathbf{R}_J|$ and U_I is the chemical hardness or Hubbard parameter of the I th atom. The first term of Eq. (11) is the long-range Coulomb interaction, and S is the short-range term that decays exponentially.²² For periodic boundary conditions, the long-range part of Eq. (10) can be evaluated using the standard Ewald summation,^{36,37} whereas the short-range part can be summed over a few neighbor periodic images of the central unit cell ($\zeta = 0$).

From Eq. (2), the external potential term, $\bar{H}_{\text{ext}}^{\mu\nu}(\mathbf{L}_\zeta)$, can be written as

$$\begin{aligned} \bar{H}_{\text{ext}}^{\mu\nu}(\mathbf{L}_\zeta) &= \langle \phi_\mu^\zeta | \hat{H}_{\text{ext}} | \phi_\nu^0 \rangle \\ &= \frac{1}{c} \mathbf{A}(t) \cdot \langle \phi_\mu^\zeta | \hat{\mathbf{p}} | \phi_\nu^0 \rangle + \frac{1}{2c^2} |\mathbf{A}(t)|^2 \bar{S}^{\mu\nu}(\mathbf{L}_\zeta), \end{aligned} \quad (12)$$

where the first term can be obtained from the expression $\langle \phi_\mu^\zeta | \hat{\mathbf{p}} | \phi_\nu^0 \rangle = -i \langle \phi_\mu^\zeta | \nabla \phi_\nu^0 \rangle = i \langle \phi_\mu^\zeta | \nabla_J \phi_\nu^0 \rangle$, ∇_J denotes the gradient with respect to atomic position \mathbf{R}_J , and $\nu \in J$ th atom.³⁸ The overlap matrix $\mathbf{S}_\mathbf{k}$ and Hamiltonian $\mathbf{H}_\mathbf{k}$ in Eqs. (5) and (6) can be calculated using Eqs. (3, 7-12). The coefficient vectors or density matrices can be updated by integrating Eq. (5) or (6), respectively. In our implementation, we use the leapfrog algorithm to integrate Eq. (6) for the k -dependent density matrix, $\mathbf{D}_\mathbf{k}$:

$$\mathbf{D}_\mathbf{k}(t + dt) = \mathbf{D}_\mathbf{k}(t - dt) + 2\dot{\mathbf{D}}_\mathbf{k}(t)dt. \quad (13)$$

One can also integrate Eq. (5) using the unitary Crank–Nicolson^{39,40} time evolution of the coefficient vectors (which we have also implemented in our code). Our resulting VG-rtTDDFTB electron dynamics simulations give the time-dependent Mulliken charge and current $\mathbf{J}(t)$:¹¹

$$\mathbf{J}(t) = -\frac{1}{2\Omega N_{\mathbf{k}}} \sum_{n\mathbf{k}}^{\text{occ.}} \mathbf{C}_{n\mathbf{k}}^\dagger(t) \mathbf{\Pi}_{\mathbf{k}}(t) \mathbf{C}_{n\mathbf{k}}(t) + c.c. = -\frac{1}{\Omega N_{\mathbf{k}}} \sum_{\mathbf{k}} \text{Tr}[\mathbf{D}_{\mathbf{k}}(t) \mathbf{\Pi}_{\mathbf{k}}(t)], \quad (14)$$

where Ω denotes the volume of the unit cell, and the elements of the current-momentum matrix is $\mathbf{\Pi}_{\mathbf{k}}^{\mu\nu}(t) = \sum_{\zeta} e^{-i\mathbf{k}\cdot\mathbf{L}_{\zeta}} \langle \phi_{\mu}^{\zeta} | \hat{\mathbf{p}} | \phi_{\nu}^0 \rangle + \frac{1}{c} \mathbf{A}(t) S_{\mathbf{k}}^{\mu\nu}$, which is a 3-component vector. The frequency-dependent conductivity, $\sigma(\omega)$, and dielectric function, $\varepsilon(\omega)$, can be derived using the time-dependent current generated by the δ -function ‘‘kick’’ field in the linear-response regime:¹¹

$$\sigma_{ij}(\omega) = \frac{1}{E_{0j}} \int_0^T e^{i\omega\tau} J_i(\tau) f(\tau) d\tau, \quad (15)$$

$$\varepsilon_{ij}(\omega) = 1 + \frac{4\pi i \sigma_{ij}(\omega)}{\omega}. \quad (16)$$

where $f(\tau) = e^{-\tau/\tau_0}$ is a filtering function with τ_0 set to 200 a.u. in this work. With these quantities calculated, the absorption spectrum is given by the imaginary part of the dielectric function $\text{Im}[\varepsilon(\omega)]$. Note that Eq. (15) does not contain any spatial dependence because of the long-wavelength approximation.³¹

3 Results and Discussion

3.1 Computational details

We first calculated the electronic ground state with SCC-DFTB using the DFTB+ package.^{22,23} The subsequent electron dynamics were then calculated with the VG-rtTDDFTB framework developed in this work. We performed electron dynamics simulations on representative chemical/material systems ranging from 0D (cluster) to 3D (bulk) geometries. Fig. 1(a) shows the optimized structure of a $(\text{H}_2\text{O})_{21}$ cluster using the TIP5P potential.^{41–43} The C_{60} and crystal silicon (c-Si) structures shown in Figs. 1 (b) and (c), respectively, were optimized with the SCC-DFTB method. The amorphous silicon (a-Si) structure containing 512 atoms in Fig. 1(d) was obtained from the last molecular dynamics step of GAP-MD

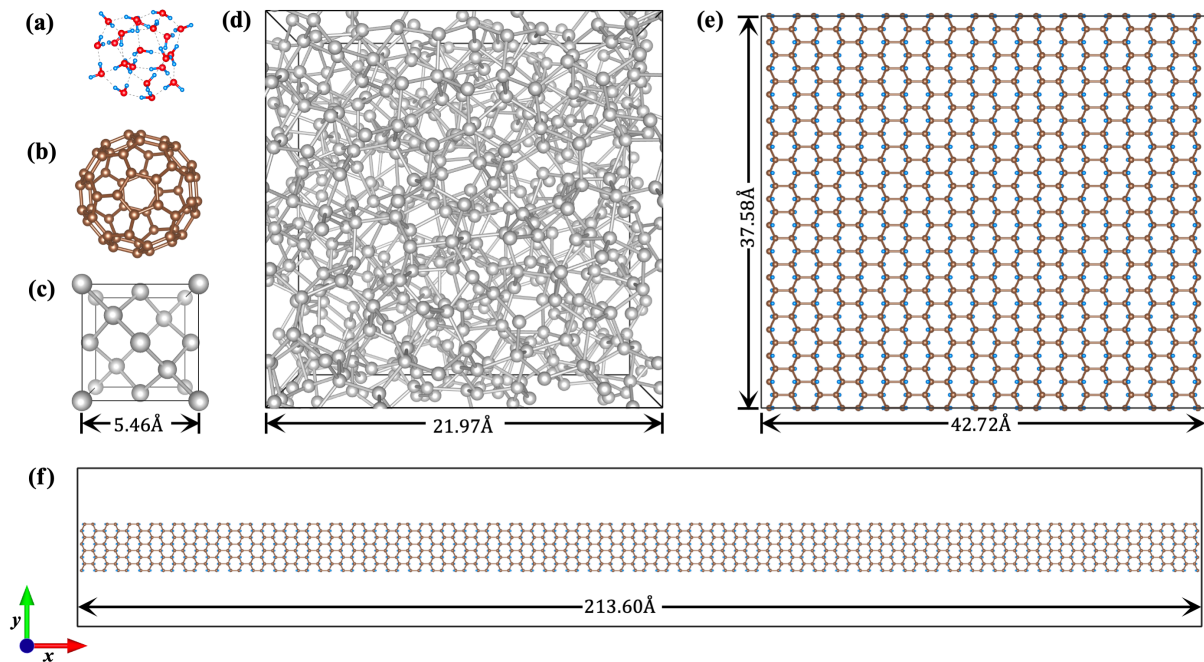


Figure 1: Molecular and periodic structures examined with our VG-rtTDDFTB approach: (a) $(\text{H}_2\text{O})_{21}$ cluster, (b) C_{60} , (c) c-Si, (d) a-Si, (e) 2D-graphane ($\text{C}_{600}\text{H}_{600}$), and (f) 1D-graphane ($\text{C}_{800}\text{H}_{800}$).

simulation with a slow quench rate (10^{11} K/s) from 1800 to 500 K,⁴⁴ which has been shown to generate reliable structures for a-Si compared to experiments.⁴⁴ For the partially periodic systems in Figs. 1(e) and (f), we built the 2D-graphane and 1D-graphane structures from the $10 \times 15 \times 1$ and $50 \times 4 \times 1$ supercells, respectively, of the boat conformer of graphane.⁴⁵ We used a 30 Å vacuum space along the nonperiodic directions for all the clusters and partially periodic systems in this work.

For our DFTB/VG-rtTDDFTB calculations, we used the *mio*²² and *pb*⁴⁶ Slater-Koster (SK) parameter sets for clustered and bulk/1D/2D systems, respectively. We found that the *siband*^{47,48} SK set for c-Si and a-Si gave more accurate electronic structures and absorption spectra. We used maximum angular momenta of *s*, *p*, and *d* for H, C/O, and Si elements, respectively. To benchmark our VG-rtTDDFT calculations, ground-state DFT and VG-rtTDDFT calculations were carried out with the real-space based OCTOPUS package^{18,19} using the Perdew-Burke-Ernzerhof (PBE) exchange-correlation functional⁴⁹ with a

0.15 Å grid spacing for c-Si. For our absorption spectra calculations, we applied a δ -pulse electric field of $E_x(t) = E_0\delta(t)$ and $E_0 = 0.005$ eV/Å applied along the x -axis at $t = 0$ for all systems. The average current is subtracted from the total current induced by the kick field to reduce noise of the optical spectra. The $16 \times 16 \times 16$ k -point meshes were generated using the Monkhorst-Pack method⁵⁰ for c-Si, and a single Γ -point was used for the calculations of the other large-scale or cluster systems. We used a 0.002 fs time step and the leapfrog integral method for all of our VG-rtTDDFTB electron dynamics simulations. Furthermore, we calculated the density of states (DOS) using a Gaussian function with a width of 0.05 eV for all cases. The Fermi level (E_f) for our DOS and band structure plots were shifted to a 0 eV reference energy. We defined our charge density using a Gaussian broadening of the atomic charges $\rho(\mathbf{r}; t) = \sum_I \frac{Q_I(t)}{\sqrt{(2\pi)^3\eta^3}} e^{-\frac{(\mathbf{r}-\mathbf{R}_I)^2}{2\eta^2}}$, where $Q_I(t) = -\Delta q_I(t)$ denotes the I th atomic charge, and η was set to 0.55 Å.

3.2 Computational Results on Large Material Systems

Table 1: Walltime for various VG-rtTDDFTB simulations (18000 steps, 36 fs) on the NERSC *Perlmutter* supercomputer.

| System | Periodicity | SK set | k mesh | number of basis functions | number of cores | Walltime (h) |
|-----------------------------------|-------------|---------------|--------------|------------------------------|--------------------|-----------------|
| (H ₂ O) ₂₁ | 0 | <i>mio</i> | 1 × 1 × 1 | 126 | 1 | 0.01 |
| C ₆₀ | 0 | <i>mio</i> | 1 × 1 × 1 | 240 | 1 | 0.06 |
| c-Si | 3 | <i>siband</i> | 16 × 16 × 16 | 72 | 64 | 0.35 |
| a-Si | 3 | <i>siband</i> | 1 × 1 × 1 | 4608 | 128 | 11.51 |
| C ₆₀₀ H ₆₀₀ | 2 | <i>pbk</i> | 1 × 1 × 1 | 3000 | 64 | 2.43 |
| C ₈₀₀ H ₈₀₀ | 1 | <i>pbk</i> | 1 × 1 × 1 | 4000 | 128 | 5.37 |

We implemented our VG-rtTDDFTB approach with a hybrid MPI/OpenMP parallelization to enable large-scale electron dynamics simulations. Our parallelization is accelerated by distributing the k -point index over MPI ranks because the electron dynamics simulation is largely independent of each k -point and requires only minimal inter-core communications. At the node level, for each k -point, the computational workloads are distributed among cores by using the multi-threaded OpenMP parallelization. To evaluate the computational

efficiency for our parallelized VG-rtTDDFTB implementation, we simulated various systems for 18000 steps (36 fs) on the NERSC *Perlmutter* supercomputer with a δ -function “kick” field. Table 1 shows that electron dynamics simulations of systems containing thousands of atoms can be efficiently performed on a modest computer cluster. These benchmarks show that our parallelized VG-rtTDDFTB implementation enables extremely efficient electron dynamics simulations of large complex condensed matter systems that are too computationally expensive with standard rtTDDFT approaches.

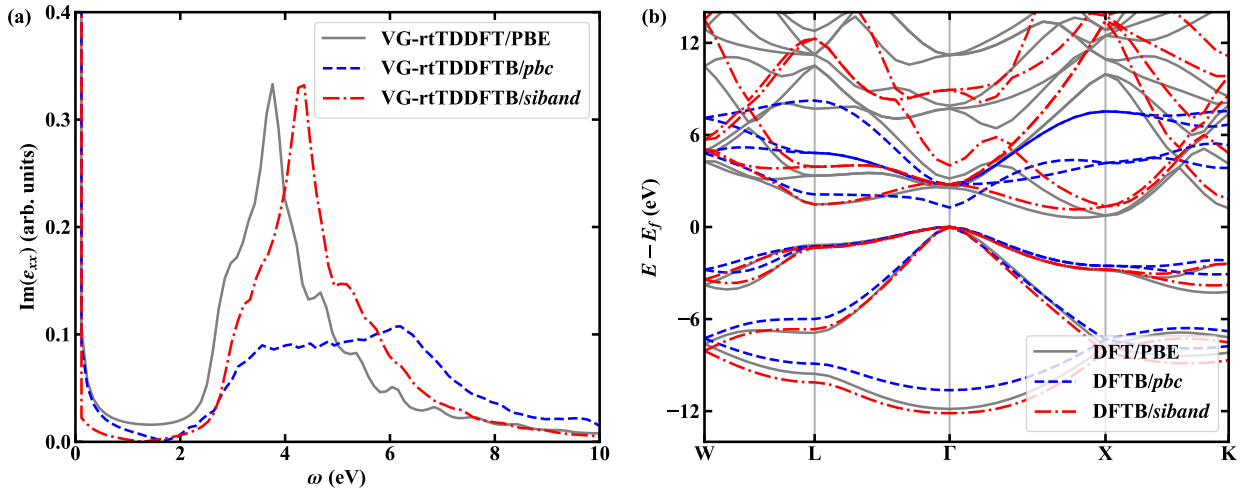


Figure 2: (a) Imaginary part of the dielectric function ϵ_{xx} and (b) electronic band structures calculated with DFT (PBE) and DFTB using the *pcb* and *siband* Slater-Koster sets for crystalline Si.

To assess the accuracy of our VG-rtTDDFTB calculations for bulk systems, the optical spectra of c-Si were calculated by our VG-rtTDDFTB using *pcb* and *siband* SK sets in comparison with that by the VG-rtTDDFT using PBE functional. As shown in Fig. 2 (a), the optical spectrum calculated by VG-rtTDDFTB using the *siband* SK file are slightly blue-shifted, and generally consistent with full VG-rtTDDFT/PBE results. The VG-rtTDDFTB optical spectrum calculated with the *pcb* parameter set, however, shows a significant discrepancy compared to the full VG-rtTDDFT/PBE results. The *siband* parameter set was specifically constructed to accurately capture the electronic structure of bulk Si,⁴⁷ which is necessary for reproducing its optical spectrum. As shown in Fig. 2(b), the DFTB band

structures for bulk Si confirm the good agreement between the *siband* parameterization and the DFT/PBE results. In contrast, the DFTB/*pb*c band structure shows narrow conduction bands and significant discrepancies compared to the DFT/PBE result.

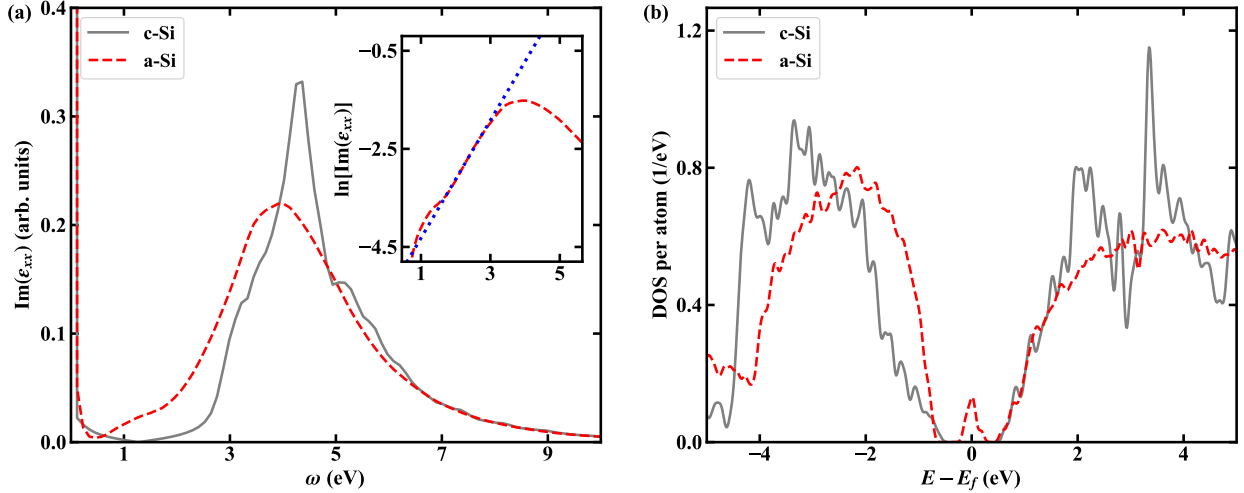


Figure 3: (a) Imaginary part of the dielectric function ε_{xx} calculated by our VG-rtTDDFTB implementation. The dotted blue line in the inset is the least-squares fitting of the Urbach region using the expression $\ln[\text{Im}(\varepsilon_{xx})] = \omega/E_U - 5.52$ with $E_U = 0.83$ eV. (b) density of states calculated with DFTB using the *siband* Slater-Koster set for c-Si and a-Si.

Amorphous silicon has been widely investigated as a noncrystalline material with applications in solar cells,⁵¹ thin-film transistors,⁵² and electrodes in batteries.⁵³ Despite its wide applicability, first-principles calculations for a-Si are rare because of the enormous computational expense of this amorphous system (which requires large supercells). To highlight the capabilities of our VG-rtTDDFTB approach, we calculate optical properties and electron dynamics for an a-Si structure shown in Fig 1(d). As shown in Fig. 3(a), the absorption edge of a-Si is broadened and slightly red-shifted compared to that of c-Si, which is generally consistent with the results reported in previous experiments.^{54–56} Furthermore, we observed a clear “Urbach” absorption edge⁵⁷ (from 1.7 to 2.8 eV) in the insert of Fig. 3(a), which arises from optical electron transitions between the localized (defected) and extended bands of the DOS shown in Fig. 3(b).

To investigate the effect of coordination defects on electron dynamics, we highlighted N -

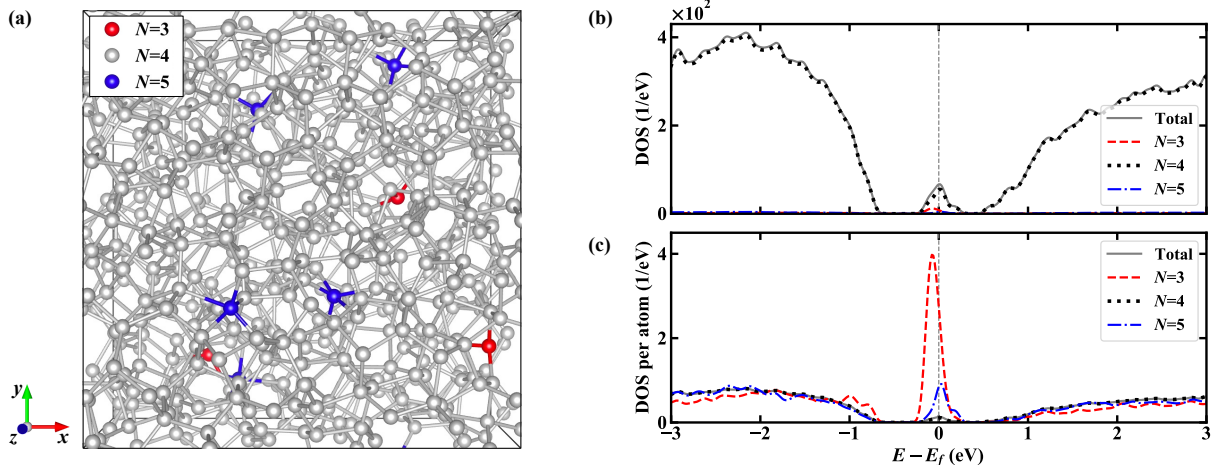


Figure 4: (a) Structure of amorphous Si containing 512 atoms with various N -coordinated atoms. Total/local (b) DOS and (c) DOS per atom for amorphous Si calculated using DFTB with *siband* Slater-Koster set.

coordinated atoms for a-Si in Fig. 4(a) as the red (3-coordinated), silver (4-coordinated), and blue (5-coordinated) balls, which were determined by the bond-length cut-off of 2.85 \AA for each atom.⁴⁴ Since 4-coordinated atoms are more prevalent (98.4% of total atoms), the effect of other coordination defects in the total and local DOS [Fig. 4(b)] are less pronounced. However, the DOS per atom in Fig. 4(c) shows that coordination defects significantly influence the electronic structure near the Fermi level of a-Si. The 3-coordinated atoms have a large peak slightly below the Fermi level due to their localized unbonded character (i.e., dangling bonded atoms), whereas 5-coordinated atoms have a small peak above the Fermi level due to extra bonding, known as “floating bonds.”^{58,59} These states near the Fermi level have a significant influence on low-energy excitations and dynamics, which result in a broadened absorption spectrum.

To further study laser-induced electron dynamics of a-Si, we used a 20 fs \sin^2 -enveloped laser pulse (centered at 10 fs) with frequencies of 2.3, 3.9, and 6.0 eV, which corresponds to the edge, peak, and tail, respectively, of the absorption spectrum of a-Si as shown in Fig. 3(a). We applied an electric field along the x -axis with an intensity of 10^{12} W/cm^2 ($E_0 \approx 0.274 \text{ eV/\AA}$) for our electron dynamics simulations. In Fig. 5, we present the instantaneous charge

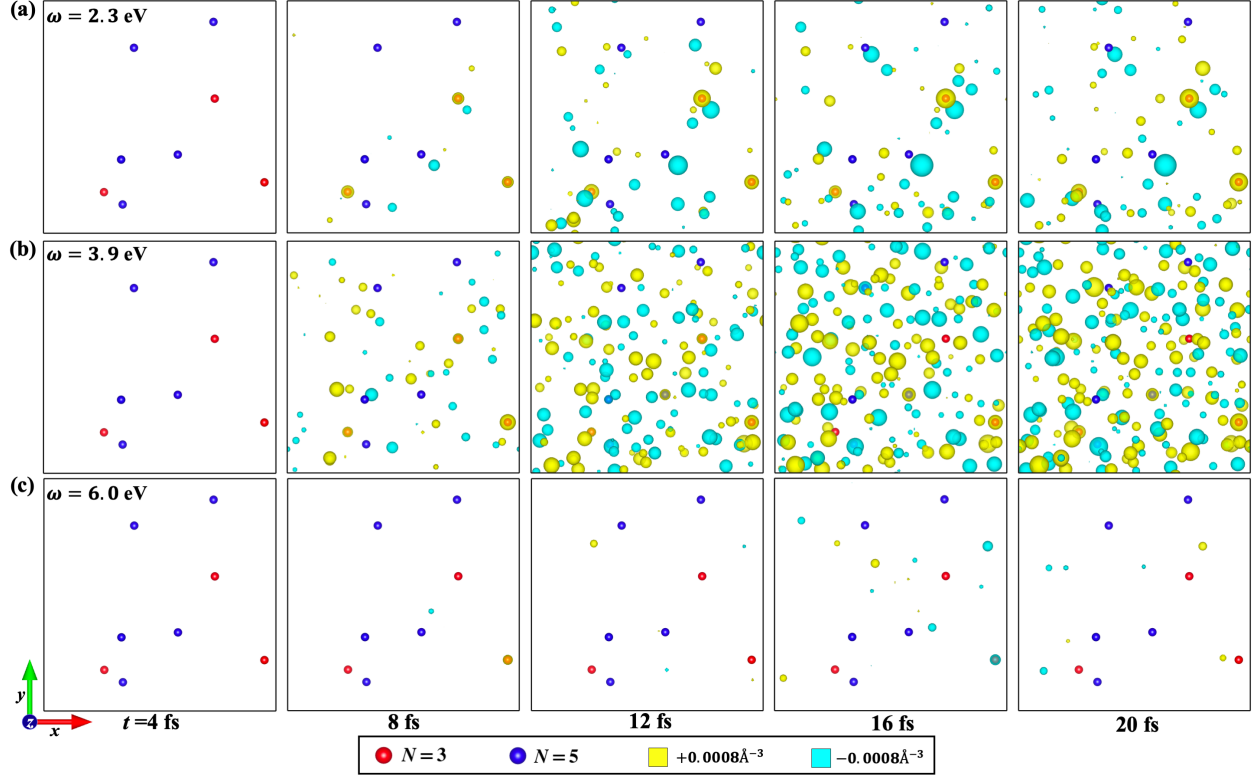


Figure 5: Snapshots of laser-induced total charge density fluctuations $\Delta\rho(\mathbf{r};t) = \rho(\mathbf{r};t) - \rho(\mathbf{r};0)$ for N -coordinated atoms with respect to the ground state at laser frequencies of (a) 2.3, (b) 3.9, and (c) 6.0 eV. The 4-coordinated atoms are not shown for clarity.

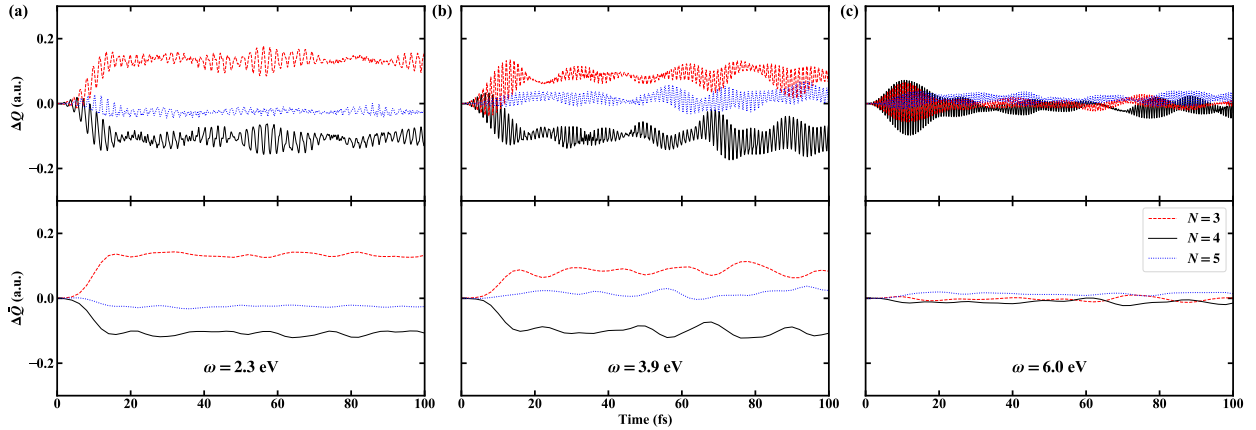


Figure 6: Laser-induced total charge evolution $\Delta Q(t) = Q(t) - Q(0)$ of various N -coordinated atoms at laser frequencies of (a) 2.3, (b) 3.9, and (c) 6.0 eV. The bottom panels depict the charge dynamics averaged every 2 femtoseconds.

density with respect to the ground state of a-Si for different laser frequencies. We see that charge transfer under different frequencies are weak in early 4 fs due to the laser pulse is turning on the stage, whereas the charge transferred tends to maximize after 12 fs. Fig. 5(a) shows that low-frequency excitations at 2.3 eV induces electron transfer among the 3- and 4-coordinated atoms. Specifically, electrons are transferred from dangling-bonded ($N = 3$) atoms for all snapshots after 8 fs. For medium-frequency excitations at 3.9 eV, Fig. 5(b) shows that more electron transfer occurs among the 4-coordinated atoms while electron transfer from 3-coordinated atoms to other atoms is still present. It is worth noting that the different floating-bonded ($N = 5$) atoms have different charge transfer modes at the same time. For high-frequency excitations at 6.0 eV, Fig. 5(c) shows that the least amount of charge transfer occurs. The 3-coordinated atoms lose electrons at 8 fs and subsequently gain charge at 16 fs. The overall electron dynamics are consistent with the absorption spectra peaks at each frequency shown in Fig. 3(a).

We calculated the Mulliken charge fluctuations among 3-, 4-, and 5-coordinated atoms with respect to the ground state as shown in Fig. 6. For low-frequency laser excitation (2.3 eV) shown in Fig. 6(a), the 3- and 5-coordinated atoms lose and gain electrons, respectively, which is consistent with the electron transfer between localized (near Fermi level) and conduction bands in the Urbach region of the absorption edge⁵⁷ as mentioned previously. For medium-frequency laser excitations (3.9 eV) shown in Fig. 6(b), the 5-coordinated atoms exhibit lose electrons, which is opposite of that shown in Fig. 6(a); in addition, electron transfer from 3-/4-coordinated atoms is weaker. These phenomena indicate that the extended valence band starts to transfer electrons to the extended conduction band. Fig. 6(c) shows that at high frequencies of 6.0 eV, the time-averaged electron transfer is relatively weak and comparable in magnitude among the N -coordinated atoms, which can be attributed to the high energy electron excitation between the extended valence and conduction bands that are far from Fermi level arising from the 4-coordinated atoms.

4 Conclusion

In summary, we have derived and implemented a new velocity gauge, real-time time-dependent density functional tight-binding (VG-rtTDDFTB) method in the open-source DFTB+ software package for electron dynamics simulations of large, condensed matter systems with periodic boundary conditions. Our VG-rtTDDFTB approach enables electron dynamics simulations of large condensed matter systems containing thousands of atoms with a favorable computational scaling as a function of system size. Our implementation uses a hybrid MPI/OpenMP parallelization scheme for massive parallelization to treat large systems on multi-core supercomputers. The computational efficiency of our VG-rtTDDFTB approach enables electron dynamics simulations of complex systems that require larger periodic supercells, such as crystal defects, complex surfaces, nanowires, and amorphous materials.

In conclusion, we have demonstrated that our VG-rtTDDFTB implementation can execute large electron dynamics for periodic systems containing thousands of atoms. As a representative example, we performed a 100-fs electron dynamics simulation for amorphous silicon (containing 512 atoms) on a modest computer cluster to study laser-induced charge transfer dynamics. Our VG-rtTDDFTB calculations give mechanistic insight into time-resolved electron density fluctuations and electron transfer as the system is irradiated in real time with electromagnetic radiation. Our simulations also allow us to analyze different electron dynamics occurring between differently-coordinated atoms at various frequencies as the system is irradiated. We anticipate that our VG-rtTDDFTB approach could find broad usage for large periodic systems, particularly for material systems that are too large to handle with rtTDDFT. Further extensions to accelerate these calculations with specialized hardware accelerators^{25,29,60} are currently underway in our group.

Acknowledgement

This work was supported by the U.S. Department of Energy, Office of Science, Office of

Advanced Scientific Computing Research, Scientific Discovery through the Advanced Computing (SciDAC) program under Award Number DE-SC0022209. This research used resources of the National Energy Research Scientific Computing Center (NERSC), a U.S. Department of Energy Office of Science User Facility located at Lawrence Berkeley National Laboratory, operated under Contract No. DE-AC02-05CH11231 using NERSC award BES-ERCAP0023692. We gratefully acknowledge Dr. Nir Goldman for providing the ChIMES-modified *siband* Slater-Koster file used to calculate VG-rtTDDFTB excited-state dynamics in this work. We gratefully acknowledge Dr. Steve D. Yang for constructing the table of contents figure used in this work.

References

- (1) Runge, E.; Gross, E. K. Density-functional theory for time-dependent systems. *Phys. Rev. Lett.* **1984**, *52*, 997.
- (2) Van Leeuwen, R. Causality and symmetry in time-dependent density-functional theory. *Phys. Rev. Lett.* **1998**, *80*, 1280.
- (3) Ullrich, C. *Time-Dependent Density-Functional Theory: Concepts and Applications*; Oxford Graduate Texts; OUP Oxford, 2011.
- (4) Yabana, K.; Bertsch, G. Time-dependent local-density approximation in real time. *Phys. Rev. B* **1996**, *54*, 4484.
- (5) Yabana, K.; Bertsch, G. Time-dependent local-density approximation in real time: application to conjugated molecules. *Int. J. Quantum Chem.* **1999**, *75*, 55–66.
- (6) Yabana, K.; Bertsch, G. Application of the time-dependent local density approximation to optical activity. *Phys. Rev. A* **1999**, *60*, 1271.

- (7) Bertsch, G. F.; Iwata, J.-I.; Rubio, A.; Yabana, K. Real-space, real-time method for the dielectric function. *Phys. Rev. B* **2000**, *62*, 7998.
- (8) Meng, S.; Kaxiras, E. Real-time, local basis-set implementation of time-dependent density functional theory for excited state dynamics simulations. *J. Chem. Phys.* **2008**, *129*, 054110.
- (9) Provorse, M. R.; Isborn, C. M. Electron dynamics with real-time time-dependent density functional theory. *Int. J. Quantum Chem.* **2016**, *116*, 739–749.
- (10) Goings, J. J.; Lestrangle, P. J.; Li, X. Real-time time-dependent electronic structure theory. *Wiley Interdiscip. Rev.: Comput. Mol. Sci.* **2018**, *8*, e1341.
- (11) Pemmaraju, C. D.; Vila, F. D.; Kas, J. J.; Sato, S. A.; Rehr, J. J.; Yabana, K.; Prendergast, D. Velocity-gauge real-time TDDFT within a numerical atomic orbital basis set. *Comput. Phys. Commun.* **2018**, *226*, 30–38.
- (12) Meng-Xue, G.; Chao, L.; Sheng, M. Real-time time dependent density functional theory with numerical atomic orbital basis set: methodology and applications. *Acta Phys. Sin.* **2018**, *67*.
- (13) Li, X.; Govind, N.; Isborn, C.; DePrince III, A. E.; Lopata, K. Real-time time-dependent electronic structure theory. *Chem. Rev.* **2020**, *120*, 9951–9993.
- (14) Yabana, K.; Nakatsukasa, T.; Iwata, J.-I.; Bertsch, G. Real-time, real-space implementation of the linear response time-dependent density-functional theory. *Phys. Status Solidi B* **2006**, *243*, 1121–1138.
- (15) Yabana, K.; Sugiyama, T.; Shinohara, Y.; Otobe, T.; Bertsch, G. Time-dependent density functional theory for strong electromagnetic fields in crystalline solids. *Phys. Rev. B* **2012**, *85*, 045134.

- (16) Mattiat, J.; Lubber, S. Comparison of Length, Velocity, and Symmetric Gauges for the Calculation of Absorption and Electric Circular Dichroism Spectra with Real-Time Time-Dependent Density Functional Theory. *J. Chem. Theory Comput.* **2022**, *18*, 5513–5526.
- (17) Bloch, F. Über die quantenmechanik der elektronen in kristallgittern. *Z. Phys.* **1929**, *52*, 555–600.
- (18) Andrade, X.; Strubbe, D.; De Giovannini, U.; Larsen, A. H.; Oliveira, M. J.; Alberdi-Rodriguez, J.; Varas, A.; Theophilou, I.; Helbig, N.; Verstraete, M. J., et al. Real-space grids and the Octopus code as tools for the development of new simulation approaches for electronic systems. *Phys. Chem. Chem. Phys.* **2015**, *17*, 31371–31396.
- (19) Tancogne-Dejean, N.; Oliveira, M. J.; Andrade, X.; Appel, H.; Borca, C. H.; Le Breton, G.; Buchholz, F.; Castro, A.; Corni, S.; Correa, A. A., et al. Octopus, a computational framework for exploring light-driven phenomena and quantum dynamics in extended and finite systems. *J. Chem. Phys.* **2020**, *152*, 124119.
- (20) Sato, S. A.; Yabana, K. Maxwell+ TDDFT multi-scale simulation for laser-matter interactions. *J. Adv. Simul. Sci. Eng.* **2014**, *1*, 98–110.
- (21) Krieger, K.; Dewhurst, J.; Elliott, P.; Sharma, S.; Gross, E. Laser-induced demagnetization at ultrashort time scales: Predictions of TDDFT. *J. Chem. Theory Comput.* **2015**, *11*, 4870–4874.
- (22) Elstner, M.; Porezag, D.; Jungnickel, G.; Elsner, J.; Haugk, M.; Frauenheim, T.; Suhai, S.; Seifert, G. Self-consistent-charge density-functional tight-binding method for simulations of complex materials properties. *Phys. Rev. B* **1998**, *58*, 7260.
- (23) Hourahine, B.; Aradi, B.; Blum, V.; Bonafé, F.; Buccheri, A.; Camacho, C.; Cevallos, C.; Deshayes, M.; Dumitrică, T.; Dominguez, A., et al. DFTB+, a software pack-

- age for efficient approximate density functional theory based atomistic simulations. *J. Chem. Phys.* **2020**, *152*, 124101.
- (24) Oviedo, M. B.; Wong, B. M. Real-time quantum dynamics reveals complex, many-body interactions in solvated nanodroplets. *J. Chem. Theory Comput.* **2016**, *12*, 1862–1871.
- (25) Allec, S. I.; Sun, Y.; Sun, J.; Chang, C.-e. A.; Wong, B. M. Heterogeneous CPU+ GPU-enabled simulations for DFTB molecular dynamics of large chemical and biological systems. *J. Chem. Theory Comput.* **2019**, *15*, 2807–2815.
- (26) Ilawe, N. V.; Oviedo, M. B.; Wong, B. M. Real-Time Quantum Dynamics of Long-Range Electronic Excitation Transfer in Plasmonic Nanoantennas. *J. Chem. Theory Comput.* **2017**, *13*, 3442–3454, PMID: 28679057.
- (27) Ilawe, N. V.; Oviedo, M. B.; Wong, B. M. Effect of quantum tunneling on the efficiency of excitation energy transfer in plasmonic nanoparticle chain waveguides. *J. Mater. Chem. C* **2018**, *6*, 5857–5864.
- (28) Kumar, A.; Ali, Z. A.; Wong, B. M. Efficient predictions of formation energies and convex hulls from density functional tight binding calculations. *J. Mater. Sci. Technol.* **2023**, *141*, 236–244.
- (29) Kumar, A.; Arantes, P. R.; Saha, A.; Palermo, G.; Wong, B. M. GPU-Enhanced DFTB Metadynamics for Efficiently Predicting Free Energies of Biochemical Systems. *Molecules* **2023**, *28*, 1277.
- (30) Ding, F.; Liang, W.; Chapman, C. T.; Isborn, C. M.; Li, X. On the gauge invariance of nonperturbative electronic dynamics using the time-dependent Hartree-Fock and time-dependent Kohn-Sham. *J. Chem. Phys.* **2011**, *135*.
- (31) Cohen, M. L.; Louie, S. G. *Fundamentals of Condensed Matter Physics*; Cambridge University Press, 2016.

- (32) Baroni, S.; Resta, R. Ab initio calculation of the macroscopic dielectric constant in silicon. *Phys. Rev. B* **1986**, *33*, 7017.
- (33) Li, P.; Liu, X.; Chen, M.; Lin, P.; Ren, X.; Lin, L.; Yang, C.; He, L. Large-scale ab initio simulations based on systematically improvable atomic basis. *Comput. Mater. Sci.* **2016**, *112*, 503–517.
- (34) Xu, Q.; Wang, S.; Xue, L.; Shao, X.; Gao, P.; Lv, J.; Wang, Y.; Ma, Y. Ab initio electronic structure calculations using a real-space Chebyshev-filtered subspace iteration method. *J. Phys.: Condens. Matter* **2019**, *31*, 455901.
- (35) Slater, J. C.; Koster, G. F. Simplified LCAO method for the periodic potential problem. *Phys. Rev.* **1954**, *94*, 1498.
- (36) Ewald, P. Evaluation of optical and electrostatic lattice potentials. *Ann. Phys.* **1921**, *64*, 253–287.
- (37) Toukmaji, A. Y.; Board Jr, J. A. Ewald summation techniques in perspective: a survey. *Comput. Phys. Commun.* **1996**, *95*, 73–92.
- (38) Bonafé, F. P.; Aradi, B.; Hourahine, B.; Medrano, C. R.; Hernández, F. J.; Frauenheim, T.; Sánchez, C. G. A real-time time-dependent density functional tight-binding implementation for semiclassical excited state electron–nuclear dynamics and pump–probe spectroscopy simulations. *J. Chem. Theory Comput.* **2020**, *16*, 4454–4469.
- (39) Crank, J.; Nicolson, P. A practical method for numerical evaluation of solutions of partial differential equations of the heat-conduction type. *Math. Proc. Cambridge Philos. Soc.* **1947**, *43*, 50–67.
- (40) Castro, A.; Marques, M. A.; Rubio, A. Propagators for the time-dependent Kohn–Sham equations. *J. Chem. Phys.* **2004**, *121*, 3425–3433.

- (41) Mahoney, M. W.; Jorgensen, W. L. A five-site model for liquid water and the reproduction of the density anomaly by rigid, nonpolarizable potential functions. *J. Chem. Phys.* **2000**, *112*, 8910–8922.
- (42) James, T.; Wales, D. J.; Hernández-Rojas, J. Global minima for water clusters (H_2O) n , $n \leq 21$, described by a five-site empirical potential. *Chem. Phys. Lett.* **2005**, *415*, 302–307.
- (43) The Cambridge Energy Landscape Database. <https://www-wales.ch.cam.ac.uk/CCD.html>.
- (44) Deringer, V. L.; Bernstein, N.; Bartók, A. P.; Cliffe, M. J.; Kerber, R. N.; Marbella, L. E.; Grey, C. P.; Elliott, S. R.; Csányi, G. Realistic atomistic structure of amorphous silicon from machine-learning-driven molecular dynamics. *J. Phys. Chem. Lett.* **2018**, *9*, 2879–2885.
- (45) Sofo, J. O.; Chaudhari, A. S.; Barber, G. D. Graphane: A two-dimensional hydrocarbon. *Phys. Rev. B* **2007**, *75*, 153401.
- (46) Sieck, A.; Frauenheim, T.; Jackson, K. Shape transition of medium-sized neutral silicon clusters. *Phys. Status Solidi B* **2003**, *240*, 537–548.
- (47) Markov, S.; Aradi, B.; Yam, C.-Y.; Xie, H.; Frauenheim, T.; Chen, G. Atomic level modeling of extremely thin silicon-on-insulator MOSFETs including the silicon dioxide: Electronic structure. *IEEE Trans. Electron Devices* **2015**, *62*, 696–704.
- (48) Markov, S.; Penazzi, G.; Kwok, Y.; Pecchia, A.; Aradi, B.; Frauenheim, T.; Chen, G. Permittivity of oxidized ultra-thin silicon films from atomistic simulations. *IEEE Electron Device Lett.* **2015**, *36*, 1076–1078.
- (49) Perdew, J. P.; Burke, K.; Ernzerhof, M. Generalized gradient approximation made simple. *Phys. Rev. Lett.* **1996**, *77*, 3865.

- (50) Monkhorst, H. J.; Pack, J. D. Special points for Brillouin-zone integrations. *Phys. Rev. B* **1976**, *13*, 5188.
- (51) Carlson, D. E.; Wronski, C. R. Amorphous silicon solar cell. *Appl. Phys. Lett.* **1976**, *28*, 671–673.
- (52) Powell, M. J. The physics of amorphous-silicon thin-film transistors. *IEEE Trans. Electron Devices* **1989**, *36*, 2753–2763.
- (53) Cui, L.-F.; Ruffo, R.; Chan, C. K.; Peng, H.; Cui, Y. Crystalline-amorphous core-shell silicon nanowires for high capacity and high current battery electrodes. *Nano Lett.* **2009**, *9*, 491–495.
- (54) Grigorovici, R.; Vancu, A. Optical constants of amorphous silicon films near the main absorption edge. *Thin Solid Films* **1968**, *2*, 105–110.
- (55) Pierce, D. T.; Spicer, W. E. Electronic structure of amorphous Si from photoemission and optical studies. *Phys. Rev. B* **1972**, *5*, 3017.
- (56) Freeman, E. C.; Paul, W. Optical constants of rf sputtered hydrogenated amorphous Si. *Phys. Rev. B* **1979**, *20*, 716.
- (57) Saito, K.; Ikushima, A. Absorption edge in silica glass. *Phys. Rev. B* **2000**, *62*, 8584.
- (58) Pantelides, S. T. Defects in Amorphous Silicon: A New Perspective. *Phys. Rev. Lett.* **1986**, *57*, 2979–2982.
- (59) Bernstein, N.; Bhattarai, B.; Csányi, G.; Drabold, D. A.; Elliott, S. R.; Deringer, V. L. Quantifying Chemical Structure and Machine-Learned Atomic Energies in Amorphous and Liquid Silicon. *Angew. Chem., Int. Ed.* **2019**, *58*, 7057–7061.
- (60) Rodríguez-Borbón, J. M.; Kalantar, A.; Yamijala, S. S. R. K. C.; Oviedo, M. B.; Najjar, W.; Wong, B. M. Field Programmable Gate Arrays for Enhancing the Speed

and Energy Efficiency of Quantum Dynamics Simulations. *J. Chem. Theory Comput.*
2020, *16*, 2085–2098.

TOC Graphic

